Macromolecules

pubs.acs.org/Macromolecules Article

Fragmentation Kinetics of Block Copolymer Micelles: Effect of Core and Corona Block Lengths

Sanghee Yang, Ali Sattari, Dongwoo Han, and Timothy P. Lodge*

Cite This: https://doi.org/10.1021/acs.macromol.4c01234 Read Online

ACCESS | Metrics & More | Article Recommendations | Supporting Information

ABSTRACT: Block copolymer molecular weight is a crucial factor influencing micelle fragmentation kinetics. In particular, it is not established how block length affects the fragmentation rate, and which block is more important. In this work, we studied the separate dependence of micelle fragmentation kinetics on core and corona block lengths, with temperature-jump experiments by dynamic light scattering. Two series of 1,2-polybutadiene-*b*-poly(ethylene oxide) (PB-*b*-PEO) were prepared: one with fixed N_{PB} (degree of polymerization of the core block) and various N_{PEO}, and the other with near constant N_{PEO} and different N_{PB}. In all, a total of nine narrow dispersity ($Đ < 1.1$) polymers were used, with PB-*b*-PEO block molar masses (in kDa) of (9−6), (9−9), (9−12), (9−13), (9−19), (15−10), (15−14), 15−17) and (15−22). Micelles were initially prepared using direct dissolution of PB-*b*-PEO in the ionic liquid 1-ethyl-3-methylimidazolium bis(trifluoromethyl sulfonyl)imide [C_2MIM][TFSI], followed by fragmentation during thermal annealing at 170 °C. The relaxation time (τ) for micelle fragmentation exhibits a power−law correlation with both N_{PB} and N_{PEO} as $\tau \sim N_{core}^{1.4} \times N_{corona}^{0.6}$. Micelles were also characterized before and after fragmentation, by small-angle X-ray scattering and by liquid-phase transmission electron microscopy. Both analyses confirmed that all micelles were spherical, and the mean aggregation numbers before and after fragmentation could be extracted. The stronger τ dependence on N_{core} suggests a higher core elastic free energy penalty due to core chain extension in the transition state, compared to the contribution of corona crowding. These results are apparently not captured by any current theory of micelle fragmentation.

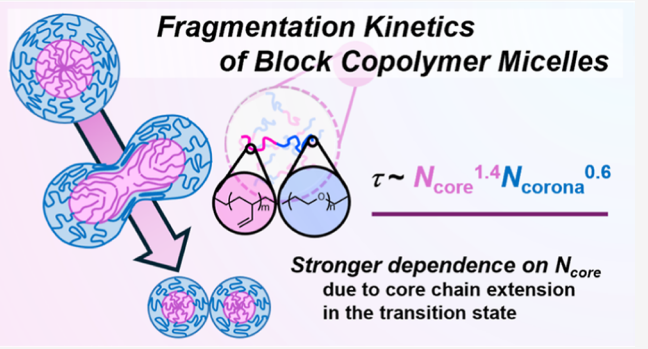

INTRODUCTION

Polymeric nanoparticles play important roles in various fields due to their exceptional versatility and customizable characteristics, with applications including biomedical imaging, sensors, energy storage, and drug delivery.[1−3] Amphiphilic block copolymers (BCPs) with contrasting solubilities can spontaneously form discrete nanostructures such as spherical micelles, cylindrical micelles, and more complex structures through solution self-assembly.[4,5] For instance, BCP micelles are widely considered as imaging agents, viscosity modifiers for motor oil, and nanoreactors.[1−3,6] Extensive theoretical and experimental studies have revealed that multiple factors, such as block chemistry, solvent type, the preparation method, and block length, can influence the resulting structures.[7] When considering other interesting applications of BCP micelles, such as drug delivery carriers, the dynamics of BCP micelles, rather than their equilibrated size and shape, also assume a pivotal role in determining effectiveness. To customize the rates of micelle dynamics for desired applications, experimental understanding of equilibration processes is also required.[8]

While external factors, including solvent quality, temperature, and concentration, significantly influence micelle dynamics, molecular properties can also impact behavior. Molecular weight (M) is a key aspect of an amphiphilic BCP influencing its structure and equilibration kinetics.[4] Generally, higher M leads to the formation of larger domains, while lower M facilitates rearrangement and self-assembly into smaller domains.[9] Furthermore, M significantly impacts the drug loading capacity and release kinetics in drug delivery.[10−12] By precisely controlling M and investigating the effect on micelle dynamics, we can gain a deeper understanding of the underlying mechanisms and inform targeted synthesis.

Micelle fragmentation or fission is a relaxation process in which a larger micelle spontaneously breaks apart into two (or more) smaller micelles, to approach the equilibrium size.[7] To fragment, the initial BCP micelles must overcome an energy barrier. Since M of polymer chains influences both the stretching energy within the micelle core and the steric

Received: May 31, 2024
Revised: August 8, 2024
Accepted: August 12, 2024

crowding in the corona, one can expect a strong M dependence on the fragmentation rate. A few reports have explored micelle fragmentation mechanisms and the M dependence of the fragmentation rates, both theoretically[13,14] and experimentally.[15,16] For example, Halperin and Alexander predicted that micelle fragmentation is mainly dominated by the core interfacial tension with a scaling of activation free energy (E_{frag}) as $E_{frag} \sim N_{core}^{2/3}$, where N_{core} is the degree of polymerization of the core block.[13] According to this model, the contribution of the corona block to fragmentation is assumed to be negligible, even for "star-like" micelles. However, Dormidontova proposed that the fusion and fragmentation times required to overcome the potential energy barrier are governed by the deformation time of the corona block.[14] As a result, this model anticipates a strong dependence of the fragmentation relaxation time on N_{corona}. Our group has investigated the M dependence of micelle fragmentation using 1,2-polybutadiene-*b*-poly(ethylene oxide) (PB-*b*-PEO) in the ionic liquid (IL) 1-ethyl-3-methylimidazolium bis(trifluoromethyl sulfonyl)imide ([C_2MIM][TFSI]). This system is favorable for isolating the process of fragmentation because the poor solvent quality for the PB core block prevents any single-chain exchange, over the course of 24 h at 200 °C.[17] We employed six different Ms of PB−PEO with a near-constant volume fraction of PEO ($f_{PEO} \approx 0.40$). Larger than equilibrium micelles ($Q/Q_{eq} > 1.5$) were prepared by a direct dissolution method and subjected to thermal annealing at 170 °C.[17−19] Using in situ dynamic light scattering (DLS), we analyzed the changes in micelle size with annealing to determine the fragmentation time. As a result, the experimental relaxation time ($\tau\tau$ displayed a significant dependence on the total degree of polymer chains (N_{total}), following an approximate scaling of $\tau \sim N_{total}^{1.8}$.[16] However, the individual dependence of the fragmentation times on N_{core} and N_{corona} were not resolved.

To address this question, this present work focuses on the effect of each block length on micelle fragmentation. We prepared two series of PB−PEOs: five PB−PEOs with a PB block of 9.3 kDa (f_{PEO} from 0.35 to 0.61) and four PB−PEOs with a PB block of 15.1 kDa (f_{PEO} from 0.33 to 0.53) by sequential living anionic polymerization,[20] followed by generation of large spherical micelles by direct dissolution. With these BCP micelles, we can resolve the individual dependence of core and corona block length on the fragmentation rate. Micelle size changes during fragmentation via thermal annealing at 170 °C are characterized by in situ DLS, small-angle X-ray scattering (SAXS), and liquid-phase transmission electron microscopy (LP-TEM).[19]

EXPERIMENTAL SECTION

Polymer Synthesis and Characterization. Table 1 lists the molecular characteristics of the two series of 1,2-polybutadiene-*block*-poly(ethylene oxide) (PB-*b*-PEO) copolymers used in this study. The copolymers were synthesized via two-step sequential anionic polymerization, briefly summarized as follows. First, the PB block was prepared with a desired molecular weight (M) by adjusting the ratio between the initiator (*sec*-butyllithium) and purified monomer (1,3-butadiene) in tetrahydrofuran (THF). During the polymerization ([monomer] < 3.0 M in THF), polymer chains were end-capped with a single ethylene oxide unit (EO, Sigma-Aldrich, ≥99.5%) resulting in hydroxyl-terminated PB blocks. The PB−OHs were dried under vacuum (<70 mTorr) at 60 °C for 3 d and characterized by a combination of size exclusion chromatography (SEC) in THF with a multiangle laser light scattering detector (Wyatt Dawn Heleos II) and

Table 1. Copolymer Characteristics

sample	$M_{n,PB}$ (kg mol^{-1})[a]	$M_{n,PEO}$ (kg mol^{-1})[a]	f_{PEO}[a]	$Đ$[b]
BO(9−6)	9.3	6.4	0.35	1.09
BO(9−9)		8.9	0.42	1.09
BO(9−12)		12.2	0.50	1.08
BO(9−13)		13.2	0.52	1.09
BO(9−19)		19.3	0.61	1.05
BO(15−10)	15.1	9.6	0.33	1.06
BO(15−14)		13.9	0.42	1.07
BO(15−17)		17.1	0.47	1.06
BO(15−22)		22.0	0.53	1.05

[a]Determined by ^{1}H NMR spectroscopy. [b]Determined from SEC-MALS in THF. BO(x−y): PB-*b*-PEO samples, where x and y denote M_n of the PB and PEO blocks (kDa).

^{1}H nuclear magnetic resonance spectroscopy (^{1}H NMR) in deuterated chloroform ($CDCl_3$, Varian Inova 500). The refractive index detector traces from SEC in THF for the two PB blocks can be found in the Supporting Information (Figures S1 and S2). The refractive index increment for PB−OH in THF (dn/dc = 0.119 mL/g) was used to obtain M from SEC in Figure S3; the two PB−OH have number-average molar masses of 9.3 and 15.1 kDa, respectively.[21] The resulting PB blocks comprised 91.5% 1,2- repeat units for 9.3 kDa and 90.4% for 15.1 kDa.

A series of PB-*b*-PEO diblocks with varying volume fractions of PEO ($0.3 \leq f_{PEO} \leq 0.6$) were synthesized by subsequent anionic polymerization of EO. Prior to the reaction, EO was purified by stirring over vacuum-dried *n*-BuMgCl (Sigma-Aldrich, 2.0 M in THF). The polymerization commenced by reinitiating the PB−OH (conc. < 1.0 M in THF) with potassium naphthalenide at room temperature. After allowing sufficient time (~30 min) for the initiation of all PB−OH chains, purified EO was added to the reaction solution, and the temperature was raised to 45 °C. After 3 d, the polymerization was terminated by adding acidic methanol. Subsequently, the reaction solvents (THF and methanol) were evaporated, and the remaining hydroxyl-terminated PB-*b*-PEO and reagents were dissolved in a minimal amount of dichloromethane. The solution was then precipitated into excess cold methanol to isolate the polymers via vacuum filtration. In the final step, the PB-*b*-PEO diblocks were freeze-dried in benzene with 0.1 wt % BHT as an antioxidant under vacuum (<70 mTorr) at 60 °C for 3 d prior to use. The samples are designated as BO(x−y), where x and y represent the number-average M (M_n) of the PB and PEO blocks, respectively, in kg mol^{-1}. To estimate the refractive index increment (dn/dc) for a diblock, the weight-average of the dn/dc for PB in THF (0.119 mL/g) and PEO in THF (0.068 mL/g) were used.[21] Finally, five BO(9-y)s were synthesized with PB−OH (M_n = 9.3 kDa), and four BO(15-y)s were also synthesized with the PB−OH (M_n = 15.1 kDa).

Micelle Solution Preparation. The polymeric micelles were prepared by inducing self-assembly of the BO diblocks in an IL. In line with previous papers,[16,18] we chose [C_2MIM][TFSI] as a selective good solvent for the PEO block to prepare micelles with a PB core and a PEO corona. [C_2MIM][TFSI] was synthesized by an anion exchange reaction[18] and characterized by ^{1}H, ^{13}C, and ^{19}F NMR spectroscopy in DMSO-d_6 (Figure S4). Via the direct dissolution method, we first annealed the freeze-dried BO diblocks in the bulk state at 70 °C for 1 h, then added [C_2MIM][TFSI] directly to produce 0.25 wt % solutions. After 1 d annealing at 70 °C, the resulting BO micelle solutions were ready for use.

Micelle Solution Characterization. DLS was used to characterize the mean hydrodynamic radius (R_h) of BO micelles and to monitor size changes during annealing. Micelle solutions before and after fragmentation were measured at 25 °C using a commercial DLS instrument comprising a Brookhaven BI-200SM goniometer, a Brookhaven BI-9000AT correlator, and a diode laser (wavelength 637 nm). The sizes of the micelles were measured with five angles (60, 80, 90, 100 and 120°). During annealing experiments, the size

https://doi.org/10.1021/acs.macromol.4c01234
Macromolecules XXXX, XXX, XXX−XXX

evolution of the micelles was measured at 170 °C using a homemade DLS instrument including a Brookhaven BI-DS photomultiplier, a Lexel Ar^+ laser (wavelength 488 nm), and a Brookhaven BI-9000 correlator. The temperature of the micellar solution was controlled to within ±0.2 °C using an index matching silicon oil bath. The determination of the mean R_h and the associated size dispersity of the micelles using DLS is outlined in the Supporting Information. To measure changes in $\langle R_h \rangle$ as a function of time during annealing, we set the temperature for the home-built instrument to 170 °C. Prior to data collection, the scattering angle was fixed to 90° and the oil bath was equilibrated to 170 °C for at least 1 h. The DLS samples were prepared by filtering through 0.45 μm PTFE syringe filters into oven-dried, dust-free glass tubes with an inner diameter of 0.51 cm and an outer diameter of 0.75 cm. The glass tubes were flame-sealed under vacuum (50 mTorr) to prevent moisture/air contamination and polymer degradation. This sealing process ensured the preservation of sample integrity during the measurements, even at 170 °C.

Small-Angle X-ray Scattering. SAXS experiments for the bulk polymers, and micelle solutions before and after fragmentation, were carried out at the Advanced Photon Source, Argonne National Laboratory, on the Sector 5−1D-D beamline of the DuPont-Northwestern-Dow Collaborative Access Team. Bulk samples were hermetically sealed in aluminum DSC pans under argon. The samples were annealed at 70 °C for 2 h prior to the measurements. The SAXS data for bulk BOs are summarized in Figure S5. BO solutions were loaded into 1.5 mm diameter borosilicate capillaries (Charles Supper Co.) and sealed with epoxy under an argon atmosphere. For each sample, two-dimensional SAXS data were collected using a Rayonix MX170-Hs CCD area detector with an 0.5 s exposure time to X-rays of wavelength 0.729 Å, keeping the sample-to-detector distance at 8.5 m. The isotropic 2D scattering data were reduced by azimuthal integration to obtain 1D scattering patterns in the form of $I(q)$ versus wavevector q. Background scattering arising from the surrounding IL and glass capillary, including an upturn at higher q resulting from nanoscale ordering in the solvent, was subtracted from the solution data. The background-corrected scattering data were analyzed using the Pedersen polymer micelle model[22,23] in SASVIEW software (Table S1).

Liquid-Phase Transmission Electron Microscopy. Estimates of the average micelle core radius $\langle R_{core} \rangle$ and associated standard deviation, σ_{core}, were also obtained by performing TEM measurements. Liquid-phase TEM was conducted on micellar solutions corresponding to the initial (before fragmentation) and final (after fragmentation) states. The imaging was performed at room temperature using an FEI Tecnai G2 Spirit Bio-Twin operating at an accelerating voltage of 120 kV with a 2k x 2k CCD camera with a spot size of 3.200 mesh copper grids coated with lacey Formvar stabilized with carbon, purchased from Ted Pella Inc., were used. Approximately 0.1 mL of micellar solution was drop-case on the grid followed by the removal of excess solution using filter paper. For each sample, around 100 individual micelles were captured and then analyzed using ImageJ software.

■ RESULTS AND DISCUSSION

To demonstrate the distinction between the newly synthesized BO diblocks and the ones used previously,[16] the core block degree of polymerization N_{PB} and volume fraction of PEO block (f_{PEO}) are compared in Figure 1. While the previous BO diblocks exhibited a nearly constant f_{PEO} of 0.4 with varying both N_{PB} and N_{PEO} (represented by gray squares), the new BO diblocks possess identical PB blocks but differing N_{PEO}, leading to $0.33 \leq f_{PEO} \leq 0.61$ (depicted by blue circles). Consequently, the investigation of micelle fragmentation kinetics using these BO diblocks enables resolution of the M dependence of each block on the process.

Characterization of as-Prepared BO Micelles. Prior to investigating the fragmentation kinetics of the BO micelles, it is important to verify the successful formation of spherical

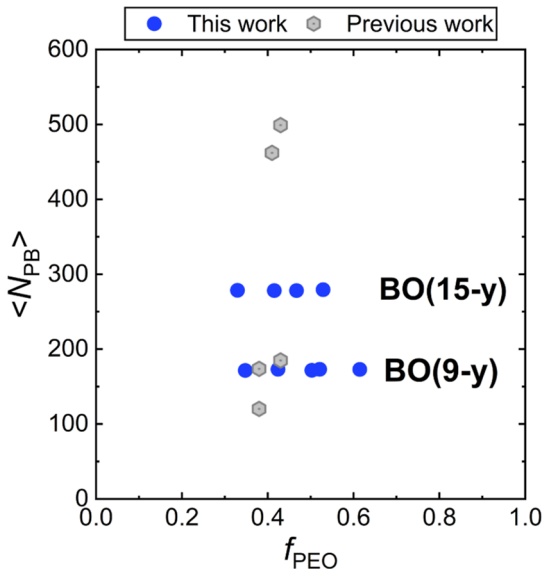

Figure 1. BO(x−y) diblocks prepared for investigating the effect of block length (blue circles), compared to BOs for the previous work (gray hexagons). BO(x−y): PB-*b*-PEO samples where x and y denote M_n of the PB and PEO blocks (kDa).

micelles. As M of each block was varied, f_{PEO} value ranged from 0.33 to 0.61, leading to different phases in the bulk state. As shown in the Supporting Information (Figures S5 and S6), most of the BOs formed a lamellar (LAM) phase in the bulk at 70 °C. However, BO(9−6) and BO(15−10), with $f_{PEO} < 0.4$, exhibited a hexagonal (HEX) phase. These compositions have the potential to form nonspherical nanoparticles, such as worm-like micelles, when in solution in a solvent that dissolves the minority block. To confirm the initial spherical micelle structures, liquid-phase TEM imaging was conducted at room temperature. Representative images for all BO micelles are presented in Figure 2. This analysis confirms that all the BO solutions indeed formed spherical micelles via the DD method at 0.25 wt % in [C_2MIM][TFSI].

Having confirmed the micelle morphologies by TEM imaging, further characterization of the micelle sizes before fragmentation was carried out using DLS and SAXS (Table 2, Figure 3). The initial average hydrodynamic radius, denoted $\langle R_h \rangle_i$, was determined by fitting the intensity autocorrelation function from DLS to a second order cumulant expansion. In the BO(9-y) series, the $\langle R_h \rangle_i$ values gradually increased from 32 to 46 nm as M_{PEO} increased from 6 to 19 kDa. Similarly, for the BO(15-y) series, the $\langle R_h \rangle_i$ values increased from 43 to 52 nm with increasing M_{PEO} from 10 to 22 kDa. When comparing the $\langle R_h \rangle_i$ of BO micelles with similar PEO block lengths, it can be observed that larger micelles were formed when increasing M_{PB}, as expected (see Table 2). Additionally, Figure S7 presents the narrow distributions of R_h obtained from REPES inverse Laplace transform analysis for all BO micelles.

Next, the average core radius of the initial micelle, $\langle R_{core} \rangle_i$, was determined through SAXS. The background-corrected scattering data were analyzed using a polymer micelle model with the Pedersen model in SASVIEW software (Table S1).[22,23] The q value at the first minimum provides an estimate of $\langle R_{core} \rangle_i$ as $\langle R_{core} \rangle \approx 4.493/q_{min}$ (Figure S9, Table S4). With the estimated $\langle R_{core} \rangle_i$, and calculated parameters such as N_{PB}, N_{PEO}, the initial average aggregation number (Q_i), we repeated fitting until achieving unchanged $\langle R_{core} \rangle_i$ (Figures

https://doi.org/10.1021/acs.macromol.4c01234
Macromolecules XXXX, XXX, XXX−XXX

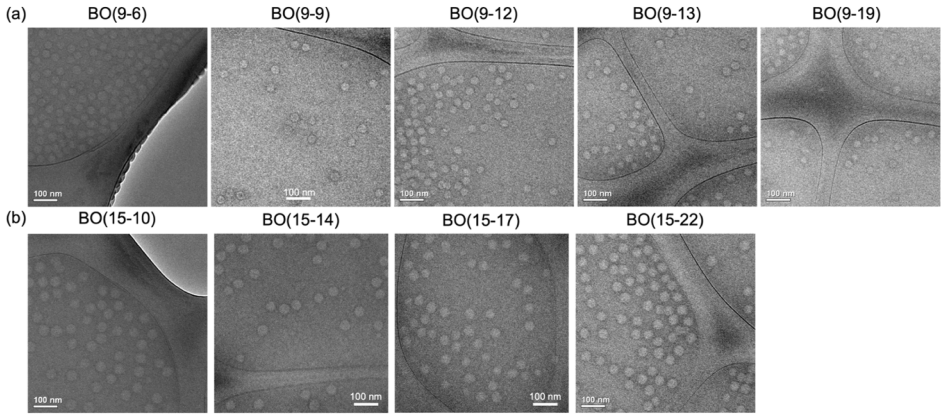

Figure 2. LP-TEM images of initial micelles for 0.25 wt % solutions of (a) BO(9-y) and (b) BO(15-y) in [C_2MIM][TFSI].

Table 2. Initial Micelle Dimensions for 0.25 wt % Solutions in [C_2MIM][TFSI]

sample	$\langle R_h \rangle_i$[a] (nm)	$\langle \mu 2/\Gamma 2 \rangle_i$[a]	$\langle R_{core} \rangle_i$[b] (nm)	Q_i[b]	$\langle R_{core} \rangle_i$ (nm)[c]	$\langle \sigma_{core} \rangle_i$ (nm)[c]
BO(9−6)	32	0.102	18.7	1540	18.1	1.4
BO(9−9)	34	0.058	18.6	1520	17.6	1.4
BO(9−12)	38	0.046	18.4	1470	17.8	1.0
BO(9−13)	40	0.060	18.5	1500	18.1	1.2
BO(9−19)	46	0.100	17.4	1250	17.4	1.9
BO(15−10)	43	0.067	24.7	2180	22.8	1.5
BO(15−14)	46	0.034	23.4	1870	21.7	1.7
BO(15−17)	48	0.062	23.0	1770	21.1	1.3
BO(15−22)	52	0.032	23.6	1920	21.6	1.3

[a]Determined from DLS at 25 °C. [b]Calculated by fitting the SAXS profiles. [c]Obtained from TEM. BO(x−y): PB-b-PEO samples where x and y denote M_n of the PB and PEO blocks (kDa).

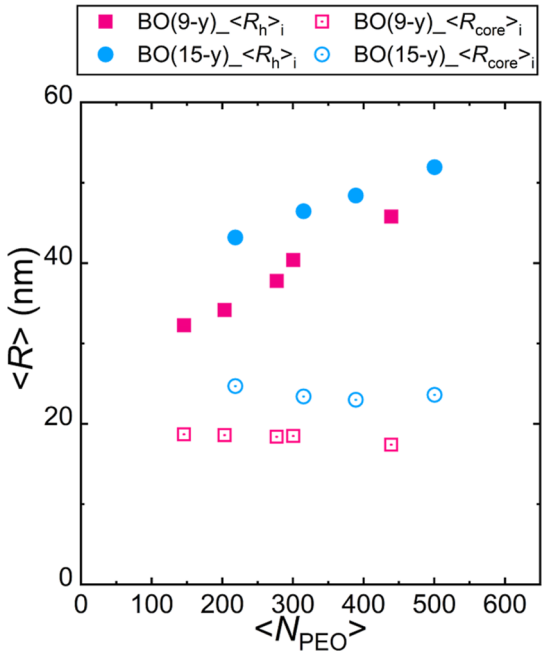

Figure 3. Dependence of $\langle R_h \rangle_i$ (filled) from DLS and $\langle R_{core} \rangle_i$ (open) from SAXS of initial micelles of BO(9-y) (pink squares) and BO(15-y) (blue circles) on the N_{PEO}. All the values are summarized in Table 2 .

S10, S11 and Table S4). In the BO(9-y) series, despite M_{PEO} varying from 6 to 19 kDa, $\langle R_{core} \rangle_i$ only experienced a small change, ranging from 18.7 to 17.4 nm. Similarly, for the BO(15-y) series, the variation in $\langle R_{core} \rangle_i$ with respect to the M_{PEO} was only 1.7 nm. This trend aligns well with the approximation of the solvent-free core, where R_{core} is predominantly influenced by N_{core}, following the scaling relationship, $R_{core} \sim N_{core}^{3/5}$.[24] As shown in Figure S12, the increase in $\langle R_{core} \rangle_i$ with N_{core} aligns with the theoretical prediction. Subsequently, the average aggregation number, Q_i, was calculated using the expression $Q = (4\pi \langle R_{core} \rangle^3)/3V_{core}$, where the core block volume V_{core} is $(M_{n,core}/\rho_{core})/N_{AV}$), and the results are summarized in Table 2.

TEM images presented in Figure 2 enable clear visualization of the micelle cores derived from the PB block, which appear bright due to their lower electron density. This makes them easily distinguishable in [C_2MIM][TFSI] without the need for staining. Therefore, through statistical analysis based on the TEM images, the micelle core size $\langle R_{core} \rangle_i$ and size dispersity can be obtained (detailed in Table 2). As with the SAXS, the TEM data show comparable average micelle core sizes for BO micelles were identical N_{PB}: the $\langle R_{core} \rangle_i$ values for BO(9-y) micelles were in the range of 17.4−18.1 nm, and those of BO(15-y) micelles ranged from 21.1−22.8 nm, with a narrow standard deviation (σ_{core} < 2 nm). The estimated $\langle R_{core} \rangle_i$ values obtained from TEM analysis closely align with those calculated from SAXS data, confirming the reliability and accuracy of the results obtained from both techniques in determining the initial micelle core sizes (Table S5).

Fragmentation Kinetics of BO Micelles by Annealing at 170 °C. Using the as-prepared, well-defined BO micelles, we investigated their fragmentation kinetics by temperature-jump experiments. The filtered micelle samples, prepared in sealed glass tubes under vacuum conditions, were monitored by DLS at 170 °C. The time-dependent average micelle size,

https://doi.org/10.1021/acs.macromol.4c01234
Macromolecules XXXX, XXX, XXX−XXX

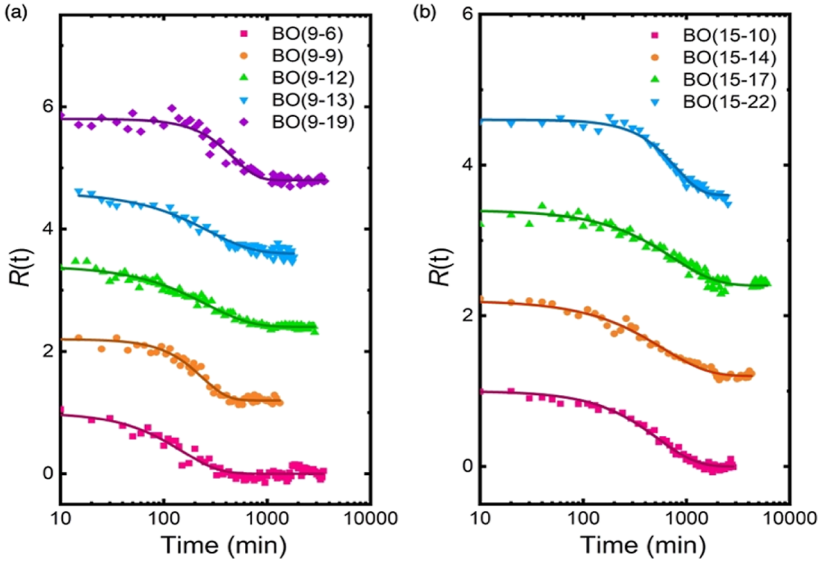

Figure 4. Time dependence of normalized $\langle R_h \rangle$, $R(t)$, for (a) BO(9-y) and (b) BO(15-y). Solid lines represent best fits to eq 1. The curves are shifted vertically for clarity.

denoted as $\langle R_h \rangle_t$, was measured in situ at regular time intervals. Considering that this is a single-angle measurement ($\theta = 90°$), there is relatively more uncertainty in each value of R_h, but nevertheless, the normalized change in radius, $R(t)$, can be employed to extract fragmentation time constants. As in previous reports, $R(t)$ was found to be well-described by a compressed exponential function.[16,18] In eq 1, both $\langle R_h \rangle_i$ and $\langle R_h \rangle_f$ correspond to the average hydrodynamic radii of the micelles before and after fragmentation. The parameter t is the annealing time, τ represents the characteristic fragmentation time, and n denotes the corresponding exponent.

$$R(t) = \frac{\langle R_h \rangle_t - \langle R_h \rangle_f}{\langle R_h \rangle_i - \langle R_h \rangle_f} = \exp[-(t/\tau)^n] \quad (1)$$

Figure 4 displays the time-dependent behavior of $R(t)$ for all BO micelle solutions. To enhance clarity, the relaxation curves for different BO micelles have been vertically shifted. An increase in the M_{PB} block from 9 to 15 kDa leads to rightward shifts in the decay curves, indicating slower kinetics. The experimental data for relaxing all BO micelles exhibit a good fit to the Avrami expression (eq 1), and the obtained kinetic parameters, t and n are summarized in Table 3. Interestingly,

Table 3. Relaxation Time, $\tau\tau$ and Exponent n Determined by T-Jump In Situ DLS

sample	τ (min)	n	sample	τ (min)	n
BO(9−6)	150 ± 8	1.2	BO(15−10)	530 ± 12	1.2
BO(9−9)	240 ± 7	1.8	BO(15−14)	590 ± 22	1.0
BO(9−12)	260 ± 7	1.0	BO(15−17)	740 ± 24	1.0
BO(9−13)	270 ± 11	1.0	BO(15−22)	790 ± 17	1.8
BO(9−19)	470 ± 19	1.9			

the fragmentation time t increases strongly with increasing M_n of both PB and PEO blocks. For instance, BO(15−22) micelles took five times longer to fragment compared to BO(9−6) micelles. A distribution of exponents from single ($n = 1$) to compressed ($n = 2$) relaxation was found, without any clear dependence on block length (Figure S14, S15).

To characterize the near-equilibrium micelles after annealing, DLS and SAXS measurements were carried out again and results are summarized in Table 4. For all BO micelles, both

Table 4. Final Micelle Dimensions after Annealing

sample	$\langle R_h \rangle_f$[a] (nm)	$\langle \mu 2/\Gamma 2 \rangle_f$[a]	$\langle R_{core} \rangle_f$[b] (nm)	Q_f	Qi/Qf
BO(9−6)	30	0.060	18	1390	1.1
BO(9−9)	32	0.050	17.7	1310	1.2
BO(9−12)	34	0.022	17.2	1210	1.2
BO(9−13)	36	0.020	17.8	1320	1.1
BO(9−19)	38	0.055	15.3	850	1.5
BO(15−10)	42	0.007	23.3	1840	1.2
BO(15−14)	43	0.044	22.7	1690	1.1
BO(15−17)	44	0.018	21.9	1520	1.2
BO(15−22)	45	0.012	20.5	1250	1.5

[a]Measured by DLS at 25 °C. [b]Calculated by fitting the SAXS profiles.

the total micelle size, $\langle R_h \rangle_f$, and associated dispersity ($\langle \mu_2/\Gamma^2 \rangle$) decreased as micelles fragmented. In the BO(9-y) micelles series, the $\langle R_h \rangle_f$ values were found to increase from 30 to 38 nm as the M of PEO block increased; however, the $\langle R_{coref} \rangle$ values obtained from SAXS were even slightly reduced from 18.0 to 15.3 nm (Table S6 and Figures S16, S17). When we compared Q_f calculated from the $\langle R_{core} \rangle_f$ with Q_i in Table 2, the decrease in Q for BO(9-y) micelles after fragmentation with increasing N_{PEO} was 11, 14, 18, 11 and 32%, which are all less than expected for complete fragmentation (i.e., if each initial micelle were to break into two). The same is true for BO(15-y) micelles, with a similar range of 10−34%. Accordingly, the calculated ratio Q_i/Q_f, also ranges from 1.1 to 1.5, consistently less than 2 (Table 4). The implication is that only a portion of each initial micelle population undergoes fragmentation, as can also be discerned from the overlap population profiles before and after annealing from DLS (Figure S20). We have confirmed that no degradation or cross-linking of BO micelles occurred during annealing at 170 °C, using SEC in THF (Figure S21). TEM imaging also confirms uniform micelle structures and the core size distribution of

https://doi.org/10.1021/acs.macromol.4c01234
Macromolecules XXXX, XXX, XXX−XXX

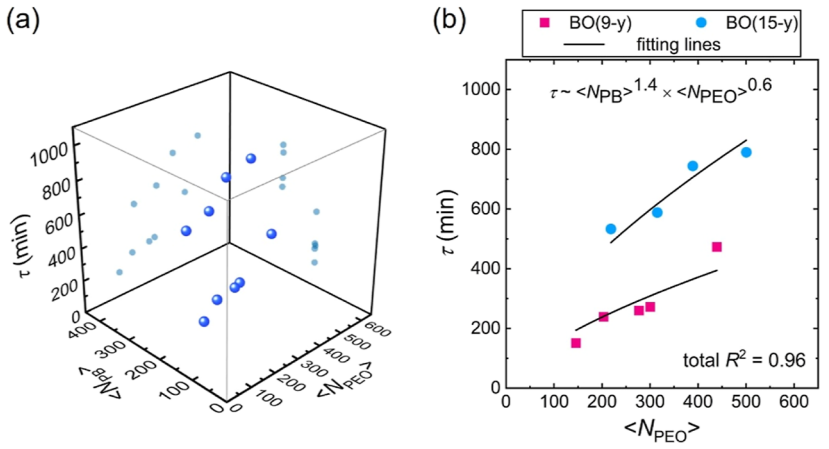

Figure 5. (a) 3D projection of $\langle N_{PB}\rangle$, $\langle N_{PEO}\rangle$ and fragmentation time (τ). (b) Dependence of τ of BO(9-y)s (pink squares) and BO(15-y)s (blue circles) on N_{PB} and N_{PEO}. Solid lines represent the best fits for all BO(x–y)s, $\tau \sim 0.007 \times N_{PB}^{1.4\pm0.2} \times N_{PEO}^{0.6\pm0.1}$ (R^2 = 0.962). BO(x–y): PB-*b*-PEO samples where x and y denote M_n of the PB and PEO blocks (kDa).

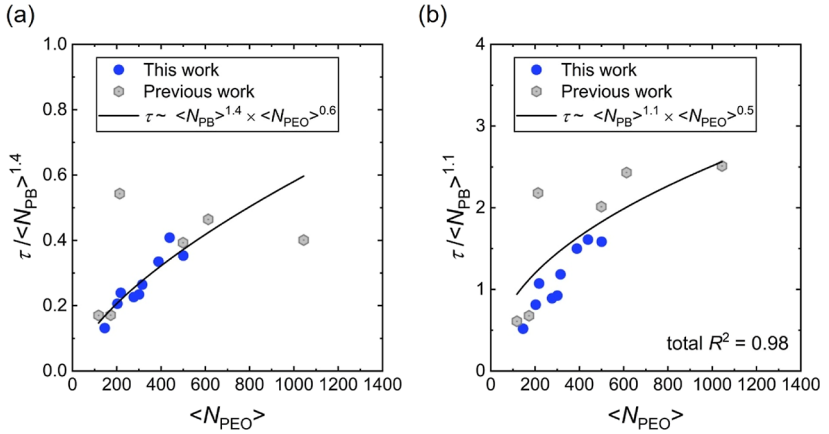

Figure 6. Combined kinetic data of previous BOs (gray hexagons) and new ones (blue circles) in this work. (a) Most of data explained well with the fitting line $\tau \sim 0.007 \times N_{PB}^{1.4\pm0.2} \times N_{PEO}^{0.6\pm0.1}$ (R_2 = 0.962), except for BO(10–9) and BO(53–46). (b) New fitting line represents the best fits for all BO(x–y)s, τ 223c; $0.11 \times N_{PB}^{1.1\pm0.3} \times N_{PEO}^{0.5\pm0.3}$ (R^2 = 0.981).

equilibrated BO micelles, consistent with the SAXS data (Figures S22, S23 and Table S7).

To quantitively analyze the dependence of fragmentation time τ on M of each block, we first present τ values versus N_{PB} and N_{PEO} in a 3D plot (Figure 5a). Clearly, τ increases with both increasing N_{PB} and N_{PEO}. Since previously it was reported that τ followed the scaling $\tau \sim N_{total}^{1.8\pm0.1}$ with BOs having a near constant $f_{PEO} \approx 0.4$, here, we fitted the data to separate power laws for both $\langle N_{PB}\rangle$ and $\langle N_{PEO}\rangle$ for all BO(x–y)s (eq 2).

$$\tau \sim A \times \langle N_{PB}\rangle^{B} \times \langle N_{PEO}\rangle^{C} \quad (2)$$

The data are well-described by power laws (Figure 5b), giving the scaling $\tau \sim \langle N_{PB}\rangle^{1.4\pm0.2} \times \langle N_{PEO}\rangle^{0.6\pm0.1}$ (Figure S24). It should be noted that the total scaling exponent is 2.0, similar to 1.8 in the previous result.[16] To confirm the reliability of the experimental scaling, we combined the new data with the previous set. When all the τ values were fit together to the specific scaling as $\langle N_{PB}\rangle^{1.4} \times \langle N_{PEO}\rangle^{0.6}$, most of the data are well described, except for two outliers (Figure 6a). If we fit the combined kinetic data together by eq 2, not using the fitting result in Figure 5b, the resulting exponents are changed slightly to 1.1 ± 0.3 for $\langle N_{PB}\rangle$ and 0.5 ± 0.3 for $\langle N_{PEO}\rangle$ with 1.6 as the total scaling exponent (Figure 6b and S26). Accordingly, we propose that the experimental scaling, $\tau \sim \langle N_{PB}\rangle^{1.4\pm0.2} \times \langle N_{PEO}\rangle^{0.6\pm0.1}$, captures the dependence of the fragmentation time on each block length.

In a previous study, we examined the total M dependence of BCP micelle fragmentation at fixed copolymer composition, and found that the fragmentation time τ scales as $N_{total}^{1.8\pm0.1}$. In light of the Dormidontova scaling theory, we tentatively concluded then that the N_{total} dependence might by dominated by the dependence on N_{corona}. In this picture the role of the corona chains in fragmentation process would be more significant than the role of the core chains, due to extreme corona crowding in the transition state. However, the present study does not support this hypothesis, where it is evident that the core block plays a significant role. To gain more insight into the stronger influence of the core block length on micelle fragmentation kinetics, it is worth comparing several previous reports on the impact of core and corona block lengths in micelle fragmentation, both for copolymers and for surfactants.

Halperin and Alexander made the first prediction of the activation free energy for BCP micelle fragmentation.[13] They suggested a negligible coronal contribution, and dominant core interfacial tension and elastic free energy of the core block, resulting in a scaling of the barrier $E_{frag} \sim N_{core}^{2/3}$. In their picture of the fusion process, E_{fusion} is primarily attributed to

https://doi.org/10.1021/acs.macromol.4c01234
Macromolecules XXXX, XXX, XXX−XXX

coronal interactions, despite being the inverse of fragmentation. Conversely, Dormidontova presented a combined scaling model for fusion and fragmentation of BCP micelles. In this analysis, fragmentation is viewed as the inverse process of fusion, thereby proceeding through the same intermediate stages. Therefore, the characteristic fragmentation time to reach the activated state is the same as that for micelle fusion. Three characteristic times associated with the fusion process are suggested: (i) micelle diffusion time, (ii) time for "deformation" of micelle coronas, and (iii) time for micelle cores to merge. Among them, coronal relaxation (ii) was considered the largest time, leading under certain conditions to the result $\tau \sim N_{corona}^{9/5}$.

As for fragmentation of surfactant micelles, pioneering experiments were done by Rharbi and Winnik,[25−27] and simulations by Pool and Bolhuis and also by Markvoort et al.[28,29] In a study of TX100 surfactant micelle fusion using fluorescent decay measurements, two energy barrier contributions to fusion were proposed: one related to coronal interactions, causing an entropic hydration barrier to close approach of the micelle cores, and the second involving micelle core rearrangements. For TX100 micelles, coronal chains interactions were found to be the primary barrier to fusion, in qualitative alignment with the prediction from Dormidontova.[26] The dependence of fragmentation rate on the M of triblock copolymers was investigated both theoretically and experimentally.[15] Analysis of the fragmentation time with respect to N_{core} was conducted using both crew-cut and starlike micelles from Pluronic polymers. The results suggested that fragmentation is primarily dominated by the core interfacial tension, in qualitative agreement with the prediction from Halperin and Alexander, with a scaling of $\ln(\tau_{frag}) \sim N_{core}^{6/5}$.[13] This work highlights the significant role of the core-forming block in the fragmentation process, and underline the importance of considering the energy barrier to fragmentation and fusion separately.

Myrhe et al. observed a surfactant-mediated fragmentation process in BCP micelles, with a strong dependence on the core block length.[30] Upon adding sodium dodecyl sulfate (SDS) as a surfactant, the short hydrophobic core block was solubilized and mixed with SDS, leading to an increase in aggregation number, and subsequent breaking into small micelles. Wu et al. investigated fragmentation kinetics in polyelectrolyte complex micelles (PEC micelles) using salt-jump or temp-jump experiments.[31] PEC micelles are multicomponent systems with positively charged blocks, negatively charged blocks, and coronal blocks, which complicate micellar dynamics. Therefore, the ionic PEC micelle cores may be fluid and contain large amounts of water (ca. 30−90%). The proposed fragmentation model consists of three successive stages: (i) changes in interfacial tension upon adding salt, (ii) separation of the swollen micelle core into two intermediate micelles with the cores in contact and the overlapping corona areas, and (iii) separation into individual micelles with the elimination of corona overlap. The core swelling (ii) was predicted to be rate-limiting because it involves the compartmentalization of the polymer chains in the core and redistribution of the corona-forming chains. Therefore, the M dependence of the micelle fragmentation relaxation time is $\ln(\tau_{frag}) \sim N_{ionic\ (core)}^{6/5}$, broadly consistent with the findings of Rharbi and Halperin.

We can also derive insight from the simulation study on the M dependence on fragmentation kinetics. Markvoort et al. simulated the fragmentation process of lipid vesicles using a coarse-grained model.[29] The study showed that tail−tail interactions in the inner vesicle layer have a more significant effect on the fragmentation rate than head−head interactions in the outer vesicle layer. The fragmentation process involves membrane deformations and perturbations, forming a neck-like or peanut-like shape, which was demonstrated in our system as well.[32] Subsequently, self-fusion of the outer monolayer completes the fragmentation. Other simulations of surfactant vesicle fragmentation also suggested that micelle fragmentation progresses through a dumbbell-like morphology, involving the formation of a long and narrow stalk with highly interdigitated surfactants.[33] This indicates that core block rearrangement in the transition state of fragmentation process may govern the activation energy barrier. It also raises the intriguing possibility of a metastable intermediate state along the fragmentation pathway, an issue that we intend to consider further in a subsequent report. In any event, all the above papers suggest that the barrier for micelle fragmentation is significantly influenced by the rearrangement of core block chains in the transition state, more so than the repulsion between corona block chains.

CONCLUSIONS

In this work, we investigated the separate effects of the two block lengths on micelle fragmentation kinetics, using a newly synthesized series of PB-*b*-PEO (BO) diblocks. Specifically, we prepared BO diblocks with varying N_{PB} and N_{PEO}, resulting in the formation of spherical micelles at 0.25 wt % in $[C_2MIM][TFSI]$. By monitoring the decrease in micelle size during annealing at 170 °C through T-jump DLS, we observed that some fraction of BO micelles undergo equilibration via fragmentation. The characteristic fragmentation times (τ), determined by fitting the normalized change in micelle size to a compressed exponential, were found to strongly depend on the molecular weight (M) of each block, where $\tau \sim \langle N_{PB}\rangle^{1.4} \times \langle N_{PEO}\rangle^{0.6}$. While there remain various views regarding the scaling of τ with respect to the M of the core and corona blocks, some theoretical models and experimental results also predicted a stronger effect of the core block length in fragmentation kinetics, as we observed here (scaling exponent $1.4 > 0.6$). This suggests that the activation energy for micelle fragmentation may be more influenced by the rearrangement of the core block chains in the elongated micelles rather than the crowding of corona block chains near the neck point of the elongated "peanut-like" micelles in transition state. In contrast to micelle fusion, where two micelles approach each other, overcome corona block repulsion, and merge, micelle fragmentation occurs when one micelle elongates its surface, rearranges the micelle core into two sphere-like volumes, and subsequently resolves the corona block repulsion to facilitate fragmentation. Consequently, the transition state in the micelle fusion process with the highest energy is likely two micelles attached together, overcoming corona block repulsion. However, the transition state in the micelle fragmentation process may involve highly elongated micelles that have to rearrange core block chains and overcome corona block repulsion, simultaneously.

ASSOCIATED CONTENT

Supporting Information

The Supporting Information is available free of charge at https://pubs.acs.org/doi/10.1021/acs.macromol.4c01234.

https://doi.org/10.1021/acs.macromol.4c01234
Macromolecules XXXX, XXX, XXX−XXX

Experimental methods; NMR spectra for all polymers; SEC traces for all polymers; NMR spectra for the IL; SAXS traces and domain spacings for bulk polymers; SAXS traces for micelle solutions before and after fragmentation, and fitting details; decay rate distributions for micelle solutions before and after fragmentation; micelle characteristics before and after fragmentation; TEM images of micelles after fragmentation, and distributions of core sizes before and after fragmentation (PDF)

AUTHOR INFORMATION

Corresponding Author

Timothy P. Lodge − *Department of Chemistry, University of Minnesota, Minneapolis, Minnesota 55455, United States; Department of Chemical Engineering & Materials Science, University of Minnesota, Minneapolis, Minnesota 55455, United States;* orcid.org/0000-0001-5916-8834; Email: lodge@umn.edu

Authors

Sanghee Yang − *Department of Chemistry, University of Minnesota, Minneapolis, Minnesota 55455, United States;* orcid.org/0000-0001-7944-6635

Ali Sattari − *Department of Chemical Engineering & Materials Science, University of Minnesota, Minneapolis, Minnesota 55455, United States;* orcid.org/0000-0001-7437-5479

Dongwoo Han − *Department of Chemistry, University of Minnesota, Minneapolis, Minnesota 55455, United States*

Complete contact information is available at: https://pubs.acs.org/10.1021/acs.macromol.4c01234

Notes

The authors declare no competing financial interest.

ACKNOWLEDGMENTS

This work was funded by the National Science Foundation Polymers Program through Award DMR-2103630. Part of this work was carried out in the College of Science and Engineering Characterization Facility, University of Minnesota, which has received capital equipment funding from the NSF through the UMN MRSEC program under Award Number DMR-2011401. Synchrotron SAXS experiments were performed at the 5-ID-D beamline of the Advanced Photon Source (APS), a U.S. Department of Energy (DOE) Office of Science User Facility operated for the DOE Office of Science by Argonne National Laboratory under contract no. DE-AC02-06CH11357. Helpful discussions with Dr Kevin Dorfman are appreciated.

REFERENCES

(1) Silvestre, C.; Duraccio, D.; Cimmino, S. Food packaging based on polymer nanomaterials. *Prog. Polym. Sci.* **2011**, *36* (12), 1766−1782.

(2) Martini, A.; Ramasamy, U. S.; Len, M. Review of Viscosity Modifier Lubricant Additives. *Tribol. Lett.* **2018**, *66* (2), 58.

(3) Bolhassani, A.; Javanzad, S.; Saleh, T.; Hashemi, M.; Aghasadeghi, M. R.; Sadat, S. M. Polymeric nanoparticles. *Hum. Vaccines Immunother.* **2014**, *10* (2), 321−332.

(4) Mai, Y.; Eisenberg, A. Self-assembly of block copolymers. *Chem. Soc. Rev.* **2012**, *41* (18), 5969−5985.

(5) Lodge, T. P. Block Copolymers: Long-Term Growth with Added Value. *Macromolecules* **2020**, *53* (1), 2−4.

(6) Feng, S.-S.; Chien, S. Chemotherapeutic engineering: Application and further development of chemical engineering principles for chemotherapy of cancer and other diseases. *Chem. Eng. Sci.* **2003**, *58* (18), 4087−4114.

(7) Lodge, T. P.; Seitzinger, C. L.; Seeger, S. C.; Yang, S.; Gupta, S.; Dorfman, K. D. Dynamics and Equilibration Mechanisms in Block Copolymer Particles. *ACS Polym. Au* **2022**, *2* (6), 397−416.

(8) Spruncken, C. C. M.; Magana, J. R.; Voets, I. K. 100th Anniversary of Macromolecular Science Viewpoint: Attractive Soft Matter: Association Kinetics, Dynamics, and Pathway Complexity in Electrostatically Coassembled Micelles. *ACS Macro Lett.* **2021**, *10* (2), 167−179.

(9) Jang, J. D.; Yoon, Y.-J.; Jeon, S.-W.; Han, Y. S.; Kim, T.-H. Molecular Weight-Dependent, Flexible Phase Behaviors of Amphiphilic Block Copolymer/Additive Complexes in Aqueous Solution. *Polymers* **2021**, *13*, 178.

(10) Riley, T.; Stolnik, S.; Heald, C. R.; Xiong, C. D.; Garnett, M. C.; Illum, L.; Davis, S. S.; Purkiss, S. C.; Barlow, R. J.; Gellert, P. R. Physicochemical Evaluation of Nanoparticles Assembled from Poly(lactic acid)-Poly(ethylene glycol) (PLA-PEG) Block Copolymers as Drug Delivery Vehicles. *Langmuir* **2001**, *17* (11), 3168−3174.

(11) Sepassi, S.; Goodwin, D. J.; Drake, A. F.; Holland, S.; Leonard, G.; Martini, L.; Lawrence, M. J. Effect of Polymer Molecular Weight on the Production of Drug Nanoparticles. *J. Pharm. Sci.* **2007**, *96* (10), 2655−2666.

(12) Mittal, G.; Sahana, D. K.; Bhardwaj, V.; Ravi Kumar, M. N. V. Estradiol loaded PLGA nanoparticles for oral administration: Effect of polymer molecular weight and copolymer composition on release behavior in vitro and in vivo. *J. Controlled Release* **2007**, *119* (1), 77−85.

(13) Halperin, A.; Alexander, S. Polymeric micelles: their relaxation kinetics. *Macromolecules* **1989**, *22* (5), 2403−2412.

(14) Dormidontova, E. E. Micellization Kinetics in Block Copolymer Solutions: Scaling Model. *Macromolecules* **1999**, *32* (22), 7630−7644.

(15) Landazuri, G.; Fernandez, V. V. A.; Soltero, J. F. A.; Rharbi, Y. Length of the Core Forming Block Effect on Fusion and Fission Dynamics at Equilibrium in PEO-PPO-PEO Triblock Copolymer Micelles in the Spherical Regime. *Macromolecules* **2021**, *54* (5), 2494−2505.

(16) Early, J. T.; Block, A.; Yager, K. G.; Lodge, T. P. Molecular Weight Dependence of Block Copolymer Micelle Fragmentation Kinetics. *J. Am. Chem. Soc.* **2021**, *143* (20), 7748−7758.

(17) Meli, L.; Lodge, T. P. Equilibrium vs Metastability: High-Temperature Annealing of Spherical Block Copolymer Micelles in an Ionic Liquid. *Macromolecules* **2009**, *42* (3), 580−583.

(18) Meli, L.; Santiago, J. M.; Lodge, T. P. Path-Dependent Morphology and Relaxation Kinetics of Highly Amphiphilic Diblock Copolymer Micelles in Ionic Liquids. *Macromolecules* **2010**, *43* (4), 2018−2027.

(19) Early, J. T.; Lodge, T. P. Fragmentation of 1,2-Polybutadiene-block-Poly(ethylene oxide) Micelles in Imidazolium-Based Ionic Liquids. *Macromolecules* **2019**, *52* (18), 7089−7101.

(20) Hillmyer, M. A.; Bates, F. S. Synthesis and Characterization of Model Polyalkane-Poly(ethylene oxide) Block Copolymers. *Macromolecules* **1996**, *29* (22), 6994−7002.

(21) Brandrup, J.; Immergut, E. H.; Grulke, E. A. *Polymer Handbook*; Wiley-Interscience: New York, 1999.

(22) Pedersen, J. S.; Svaneborg, C. Scattering from Block Copolymer Micelles. *Curr. Opin. Colloid Interface Sci.* **2002**, *7*, 158−166.

(23) Pedersen, J. S.; Svaneborg, C.; Almdal, K.; Hamley, I. W.; Young, R. N. A Small-Angle Neutron and X-ray Contrast Variation Scattering Study of the Structure of Block Copolymer Micelles: Corona Shape and Excluded Volume Interactions. *Macromolecules* **2003**, *36* (2), 416−433.

(24) Ma, Y.; Lodge, T. P. Poly(methyl methacrylate)-block-poly(n-butyl methacrylate) Diblock Copolymer Micelles in an Ionic Liquid: Scaling of Core and Corona Size with Core Block Length. *Macromolecules* **2016**, *49* (9), 3639−3646.

(25) Rharbi, Y.; Winnik, M. A.; Hahn, K. G. Kinetics of Fusion and Fragmentation Nonionic Micelles: Triton X-100. *Langmuir* **1999**, *15* (14), 4697−4700.
(26) Rharbi, Y. Fusion and Fragmentation Dynamics at Equilibrium in Triblock Copolymer Micelles. *Macromolecules* **2012**, *45* (24), 9823−9826.
(27) Rharbi, Y.; Karrouch, M.; Richardson, P. Fusion and Fission Inhibited by the Same Mechanism in Electrostatically Charged Surfactant Micelles. *Langmuir* **2014**, *30* (27), 7947−7952.
(28) Pool, R.; Bolhuis, P. G. Prediction of an Autocatalytic Replication Mechanism for Micelle Formation. *Phys. Rev. Lett.* **2006**, *97* (1), 018302.
(29) Markvoort, A. J.; Smeijers, A. F.; Pieterse, K.; van Santen, R. A.; Hilbers, P. A. J. Lipid-Based Mechanisms for Vesicle Fission. *J. Phys. Chem. B* **2007**, *111* (20), 5719−5725.
(30) Myhre, S.; Amann, M.; Willner, L.; Knudsen, K. D.; Lund, R. How Detergents Dissolve Polymeric Micelles: Kinetic Pathways of Hybrid Micelle Formation in SDS and Block Copolymer Mixtures. *Langmuir* **2020**, *36* (43), 12887−12899.
(31) Wu, H.; Ting, J. M.; Tirrell, M. V. Mechanism of Dissociation Kinetics in Polyelectrolyte Complex Micelles. *Macromolecules* **2020**, *53* (1), 102−111.
(32) Early, J. T.; Yager, K. G.; Lodge, T. P. Direct Observation of Micelle Fragmentation via In Situ Liquid-Phase Transmission Electron Microscopy. *ACS Macro Lett.* **2020**, *9* (5), 756−761.
(33) Sammalkorpi, M.; Karttunen, M.; Haataja, M. Micelle Fission through Surface Instability and Formation of an Interdigitating Stalk. *J. Am. Chem. Soc.* **2008**, *130* (52), 17977−17980.

https://doi.org/10.1021/acs.macromol.4c01234
Macromolecules XXXX, XXX, XXX−XXX